POAC'25
St. John's, Newfoundland and Labrador, Canada

Proceedings of the 28th International Conference on Port and Ocean Engineering under Arctic Conditions
Jul 13-17, 2025
St. John's, Newfoundland and Labrador
Canada

Full-scale measurements of deflection and stresses in floating sea ice subjected to long-term concentrated load

Aleksey Marchenko, Aleksey Tanurkov
The University Centre in Svalbard, Longyearbyen, Norway

ABSTRACT

A full-scale experiment on long-term sea ice loading was conducted in the Vallunden lagoon of the Van Mijen fjord in Spitsbergen. Sea ice of 80 cm thickness was loaded onto a 4.5 t bandvagn over 30 h. Before the bandvagn arrived at the experimental site, four ice pressure cells, acoustic transducer, and two temperature strings were installed on the ice. Vertical ice displacements were measured using water pressure sensors attached to the ice with wires at three points. The recorded pressures values in ice and water gave a good indication of the start and the end of the load. Acoustic activity was recorded during loading and subsequently due to thermal deforming of the ice caused by the changes in air and ice temperature. Based on water pressure data, long-term changes in the shape of the ice sheet during the experiment were analysed. Numerical modeling of the experiment in Comsol Multiphysics software showed that the simulated deflections and radial stresses of ice are similar to the measured deflections and pressures in the ice.

KEY WORDS: sea ice, bearing capacity, viscoelastic properties, numerical simulations

INTRODUCTION

The long-term bearing capacity of floating ice cover is complicated by creep effects that severely limit the applicability of traditional, stress-based theories of failure (Betlaos, 2002). Kerr (1996) referred 52 papers where creep properties of floating ice subjected static load of long duration were discussed. Stages of ice deformations in creep are usually subdivided on primary, secondary and tertiary creeps following each other with time (Schulson and Duval, 2009). The last tertiary stage of creep ends with the ice failure. Depending on the temperature and the applied load, secondary and tertiary creep stages can be reached after a very long time.

The creep rupture limit tends to very small values with increasing time.

Most of experiments on ice creep were performed with uniaxial loading of ice cores in tension or compression. Physical basis for the creep of granular freshwater ice and the fall-off effect of the power law exponent from $n = 3$ to the values close to 1 at high temperatures were discussed in numerous papers (Sinha, 1978; Cole, 2020). The predominant deformations of floating ice subjected to local load are bending deformations, which, depending on the distance from the loading area and the vertical coordinate, manifest themselves as pure compression or tension. In addition, temperature and salinity gradients across the ice thickness influence the vertical profile of the elastic characteristics of ice (Kerr and Palmer, 1972) and the viscous properties of ice (Marchenko et al, 2021). Nevel (1966) considered Maxwell ice creep model and assumed that ice is incompressible with the Poisson's ratio of 0.5 to calculate the shape of floating ice subjected concentrated loading. The latter assumption made it possible to simplify the equations describing the bending deformations of floating ice. The axially symmetric analytical solution was constructed for a uniform load distributed over a circular area of given radius. According to the solution, the ice deflection increases proportionally to $\sqrt{t}$ for relatively short times, and then the asymptotic behaviour becomes linearly dependent on time t.

Vaudrey (1978) carried out several field tests on sea ice of thickness 50-60 cm loaded with 3.4 t distributed over a rectangular area of 1.5x4 m. The surface ice temperature changed from -8C to -30C during tests. Tests performed during 80-90 h demonstrated the dependences of ice surface elevation from time similar $\sqrt{t}$ during first 5-7 h of the test, then the ice deflection increased with time linearly. No radial or circumferential cracking was observed. Ice deflections were measured beneath the load by means of a manometer containing antifreeze and radially outward from the load by taking level readings. Finite element simulations were performed using relaxation functions obtained in the field tests with floating cantilever beams carried out in the same location and in the laboratory tests on 3 points bending of ice beams. The relaxation function prescribes dependence of the effective elastic modulus from time. The relaxation functions were obtained from the tests with different temperatures.

Betlaos (2002) described results of 42 breakthrough tests performed on freshwater lake ice with thickness smaller 50 cm, and on sea ice with thickness changing from 50 cm to 1.9 m in 1973-1975. The ice thickness changed from 6 to 60 cm, and the ice temperature was in the range from -0.4°C to -19°C. Sea ice salinity varied from 4 ppt to 15 ppt. Most of the breakthrough tests were of two types, either ramp load to failure, or ramp load followed by constant load. There were also a few tests with stepped load application, comprising more than one ramp or constant load levels. Time to ice failure in most of the tests was smaller 8 h, in several tests time to failure was smaller 1 h. The creep effect was well visible on ramp load tests lasting under 1 h. The strain energy criterion for failure of floating ice sheets was confirmed using test results (Betlaos, 1978). It was noted that many of the tests did not achieve breakthrough, either by accident or by design. Though such tests are very useful in studying creep response, they are not considered in the paper.

In the present paper we describe results of the field test conducted on sea ice in the Vallunden lagoon of the Van-Mijen Fjord, Spitsbergen, from March 31 to April 1, 2022. The ice was loaded with a bandvagn (BV, https://en.wikipedia.org/wiki/Bandvagn_206) of 4.5 t weight during 30 h. We measured deflection of ice in three points, in-plane ice stresses in four locations, acoustic emission and temperature. Ice samples taken from the experimental site were used in the laboratory tests on stress relaxation. The elastic modulus and the Poisson's ratio of ice were calculated from measurements of the p-wave speed and the eigen frequency of floating vibrating ice beams. Finally, we modelled the flexural deformation of floating ice under

concentrated load using finite element software Comsol Multiphysics and Maxwell ice creep rheology.

FIELD EXPERIMENT

The field experiment was conducted in the Vallunden lagoon in the Van-Mijen Fjord near Svea, Spitsbergen, from March 31 to April 1, 2022. The width of the lagoon width varies from 300 m to 750 m, and the length is about 1200 m (Fig. 1). The sea ice in the lagoon was S2 type with columns 2-3 cm in diameter. The ice thickness was 80 cm, the mean salinity was 5 ppt. The snow thickness varied from 5 cm to 20 cm.

Figure 1. Location on the bandvagn on sea ice in Vallunden lagoon (https://toposvalbard.npolar.no/ , 77.88282ºN, 16.77496ºE).

BV of 4.5 t weight was at the test site (Fig.1) from 9:40 UTC, March 31, to 16:10 UTC, April 1, 2022. Before BV was placed at the test site, four ice pressure cells Geokon (IP1-IP4) were frozen in the ice at 20 cm distance from the ice surface to measure in-plane radial stresses in ice, three Sea Beard 39 Plus water pressure sensors (WP1-WP3) were attached to the ice with wires to measure water pressures at specific depths below the ice, two temperature strings GeoPrecision (TS1,TS2) were frozen into the ice to measure ice and air temperature with spatial resolution of about 5 cm near BV (TS1) and on 100 m distance from BV (TS2), and acoustic transducer PK15I – 150 kHz with low-power integral preamplifier was frozen in the ice near ice pressure sensor IP1. Acoustic transducers recorded emission with Mistras Micro-SHM system. After all sensors were deployed, BV arrived at the experimental site and left there for ~30 h. The locations of the sensors are shown in Fig. 2. Sampling intervals of ice pressure sensors, water pressure sensors, and temperature strings were set respectively to 10 s, 0.5 s, and 10 min. Water pressure and air/ice temperatures were measured during ~35 h. Ice pressures and acoustic emission were measured only during the first 9 h of the experiment due to battery capacity.

Water pressure sensors are sensible to both changes in water pressure and changes in atmospheric pressure. Therefore, we analyse the difference between water pressure recordings made in three different locations, assuming that the distance between the ice bottom and the pressure sensors did not change during the experiment. Figures 3a and 3b show the differences between pressures recorded by sensors WP1 and WP2 (Δh_{12}), and WP1 and WP3 (Δh_{13}) versus time. Figure 3b shows the monotonic increase of the vertical distances Δh_{12} and Δh_{13} during

approximately the first 8 h of the experiment at different rates. Then, the rates turned to zero for ~5 h, after which the distances Δh_{12} and Δh_{13} decreased (Fig. 3a). Figures 3c and 3d shows respectively shocks in Δh_{12} and Δh_{13} in the times when BV arrived and left from the experimental site.

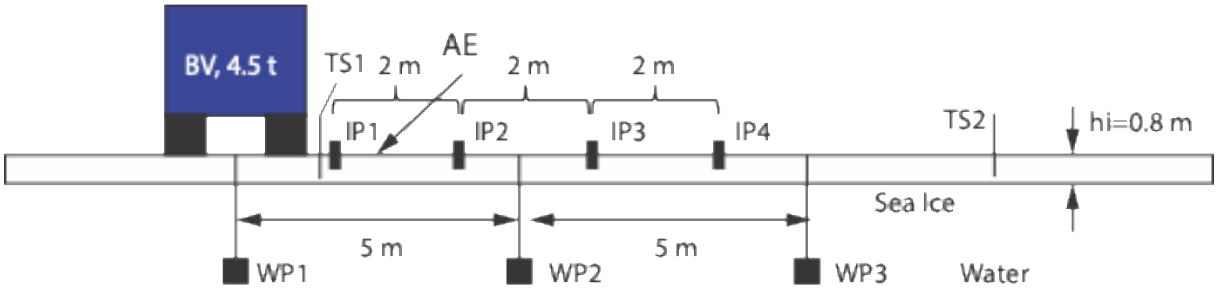

Figure 2. Deployment schematic of ice pressure sensors (IP1-IP4), water pressure sensors (WP1-WP3), thermistor string (TS1, TS2) and acoustic emission sensors (AE) near BV. Not to scale.

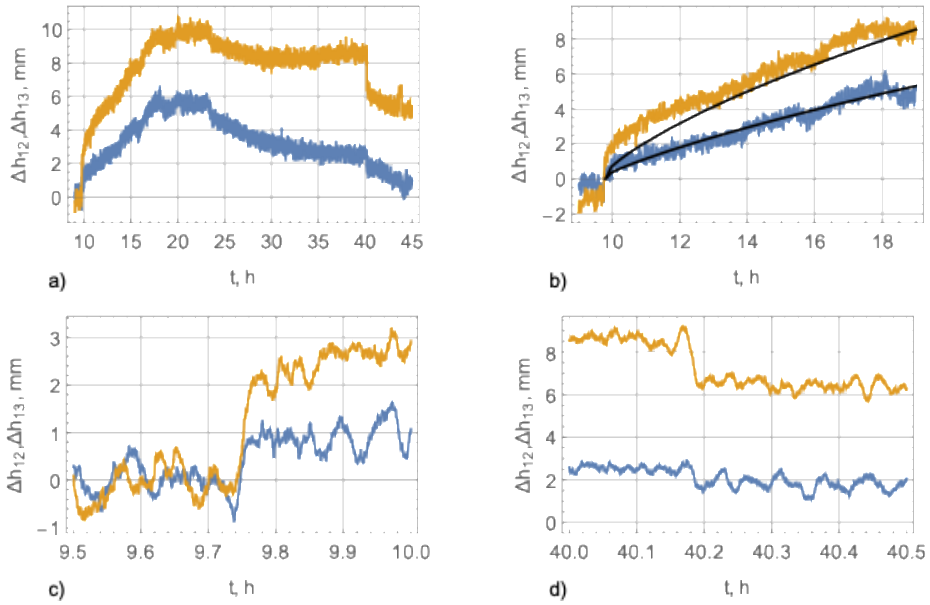

Figure 3. Difference of water pressures measured by sensors WP1 and WP2 (blue lines) and sensors WP1 and WP3 (yellow lines) versus time over entire time of the recording (a), during the first 9 hours (b), and upon the BV's arrival (c) and departure (d) from the test site. Solid black lines are reconstructed from the results of numerical simulations (b). The time is calculated from 00:00 UTC, March 31, 2022.

The broken lines consisting of two straight segments shown in Figure 4 approximate the ice shape for each hour depending on time. The broken lines extend from $r = 0$ to $r = 10$ m and have a corner point at $r = 5$ m. Points with coordinates $r = 0$, $r = 5$ m, and $r = 10$ m correspond to the locations of sensors WP1, WP1, and WP3 (Fig. 2). The vertical coordinates of these points are equal to $-\Delta h_{13}$, $-\Delta h_{23}$, and 0, where $\Delta h_{23} = \Delta h_{13} - \Delta h_{12}$. In reality, the ice deflection at $r = 10$ m is not equal to zero. Figure 4a shows the increase of ice deflection below BV at $r = 0$ from 1 mm to 8 mm during the first 9 hours of the experiment. The increase

of ice deflection at $r = 5$ m was only 2 mm over the same time. Figure 4a shows the reduction in the area of deformed ice towards the origin over this time. Figure 4b shows that by the time $20\text{h} < t < 28\text{h}$ the shape of the ice did not change significantly, while the ice deflection at $r = 0$ decreased from 8 mm to 6 mm. Then, the deflections increased at $r = 0$ and $r = 5$ m, so that the broken line illustrating the shape of the ice became straight at $t = 39$ h. The ice deflection decreased from 6.6 mm to 4 mm at $r = 0$ and from 4 mm to 2 mm at $r = 5$ m when BV left the research site at $t \approx 40.16$ h. The decrease in ice deflection at $r = 0$ affected the localisation of ice deformations near the origin at $40 < t < 43$ h, but at $t = 45$ h the ice became practically flat at $0 < r < 5$ m, and the area of bending deformations turned into a ring located at $r > 5$ m.

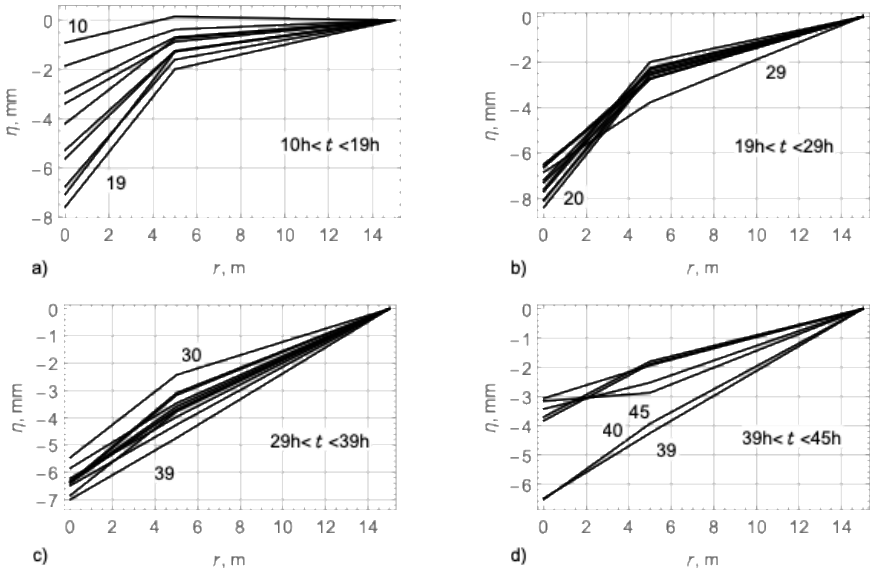

Figure 4. The broken lines approximate ice shape for each hour depending on time. The time pointed out in the figures is calculated from 00:00 UTC, March 31, 2022.

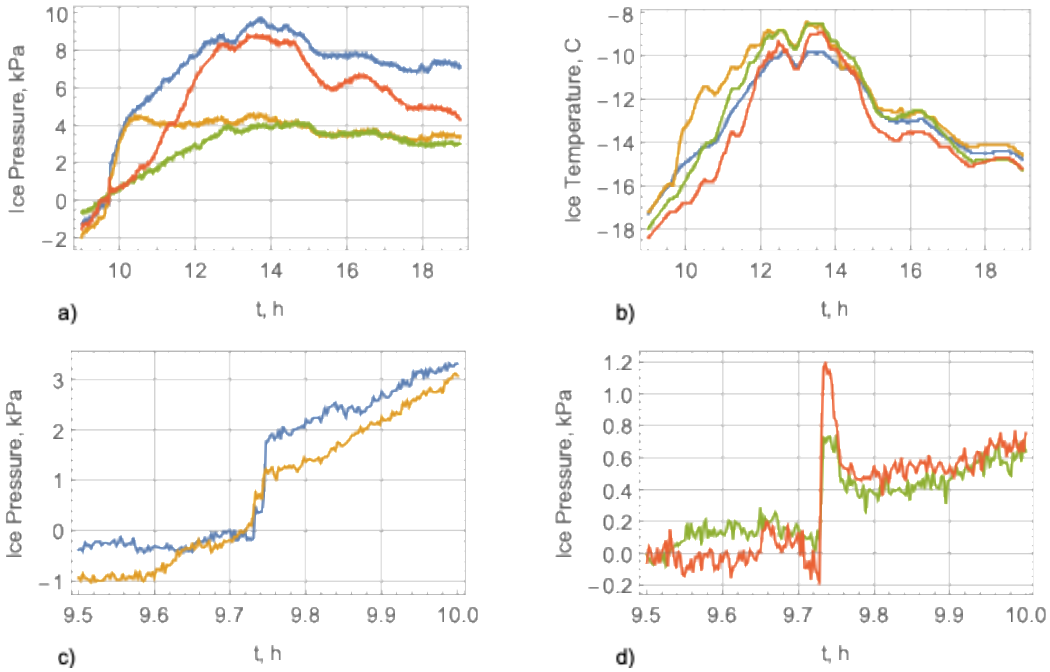

Figure 5. (a) In-plane ice pressures measured on 20 cm depth in ice by pressure cells IP1 (blue), IP2 (yellow), IP3 (green), and IP4 (red) versus time during the first 9 hours of the experiment. (b) Temperatures versus time measured by temperature sensors mounted together with ice pressure cells IP1-IP4 near the ice surface. (c, d) Ice pressures measured by pressure cells IP1 (blue), IP2 (yellow) (c) and IP3 (green), IP4 (red) (d) upon the BV's arrival at the test site. The time is calculated from 00:00 UTC, March 31, 2022.

Figure 5a shows show the pressures recorded by ice pressure sensors IP1-IP4 during the first 9 hours of the experiment versus time. Figures 5c and 5d show respectively the shocks in the ice pressures IP1, IP2 and IP3, IP4 upon arrival of BV to the experimental site. Figure 5b shows the temperatures measured versus the time by the temperature sensors mounted together with ice pressure sensors IP1-IP4 near the ice surface. The ice pressure recorded by IP1 increased by 2 kPa upon the BV's arrival at the test site (Fig. 5c). The amplitudes of pressure shocks recorded by the other sensors IP2-IP4 were smaller (Fig. 5c and 5d). The ice pressure data (Fig. 5a) and the ice temperature data (Fig. 5b) correlate with each other. Therefore, we assume that the changes in the ice pressure were caused by thermal deformations of the ice due to weather changes, with exception of sharp changes of the pressure associated with the arrival of BV at the test site around 9:43 UTC on March 31, 2022.

Figure 6a shows temperature profiles in the ice and in the air above the ice measured by temperature strings TS1 (black points) and TS2 (grey points). One can see that temperature profiles in the ice ($0 < z < 80$ cm) are stable, while the air temperature ($z > 80$ cm) demonstrates significant fluctuations from -9°C to -26°C. Temperatures of the ice measured by TS1 and TS2 near ice bottom at $0 < z < 30$ cm were similar. The upper 50 cm of ice was colder near BV. Figure 6b shows the mean ice temperatures averaged over the ice thickness at the points where TS1 and TS2 were installed. Depending on time the mean temperature of ice near BV was lower the mean temperature of ice on 100 m distance from BV by 0.5-1.5°C. The effect can be explained by a thinner snow layer near BV and a shadow from BV preventing solar radiation from affecting the ice. The ice began to cool at 13:00 (Fig. 6b), and the ice pressure began to decrease synchronously (Fig. 5a). The ice temperature measured by TS2 began to increase after 23:00 UTC, March 31. This correlates with the decrease in h_{12} and h_{13} at this time (Fig. 3a). Changes in ice temperature likely influenced thermal deformations of ice and changes in ice deflection shown in Fig. 4b and 4c.

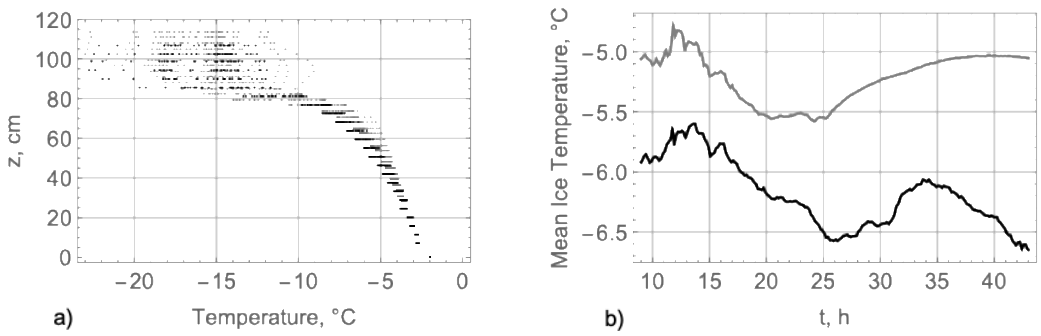

Figure 6. (a) Vertical profiles of temperatures recording each hour through the ice thickness and in the air by temperature string TS1 (black points) and TS2 (grey points) from 9:00 UTC, March

31, to 16:00 UTC, April 1, 2022. Ice bottom is at $z = 0$, and ice surface is at $z = 80$ cm. (b) The mean ice temperatures recorded by TS1 (black line) and TS2 (grey line) versus time over entire time of the recording. The time is calculated from 00:00 UTC, March 31, 2022.

Figure 7a shows the accumulated number of acoustic hits near BV. The largest number of them occurred in the first hour after the BV arrived at the test site from 9:40 to 10:40 UTC, as well as after 13:00 UTC, when the cooling of the ice due to weather change influenced the formation of thermal cracks. The amplitudes of acoustic hits caused by thermal deformations of ice were significantly smaller than the amplitudes of acoustic hits caused by the impact of BV on ice (Fig. 7b). Figures 7c and 7d show the largest acoustic hits registered during the arrival of BV at the test site.

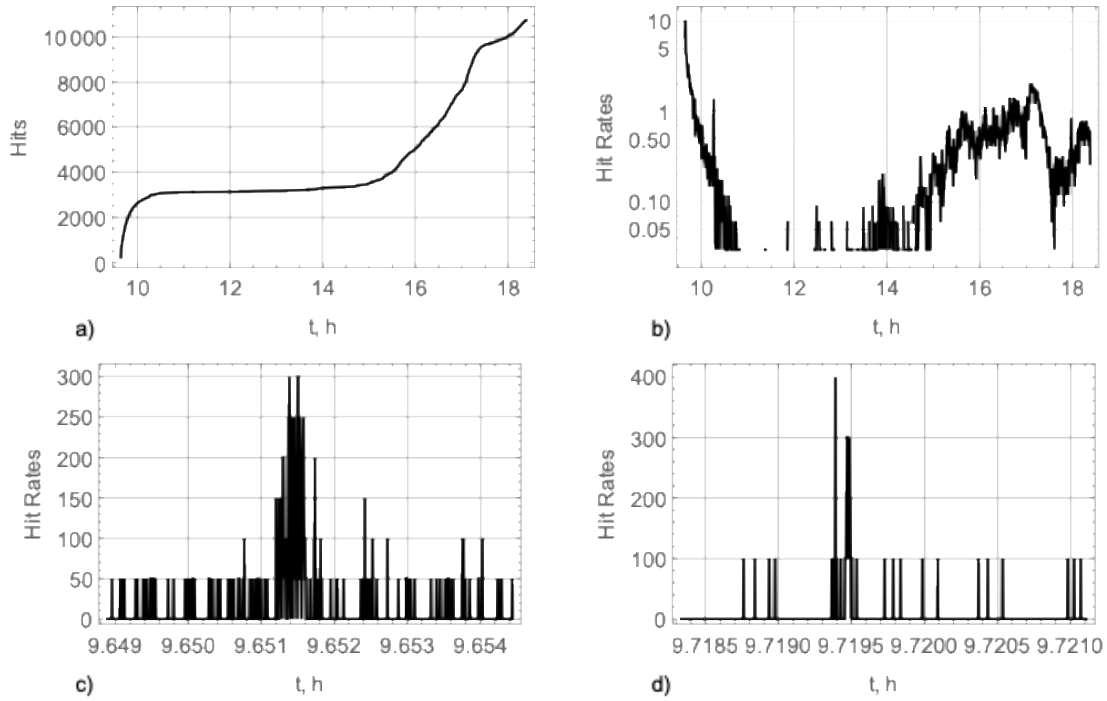

Figure 7. The cumulative number of acoustic hits (a) and the hit rate (b) versus time recorded near BV. The first (c) and the second (d) events of hit rates recorded during the arrival of BV at the test site. The time is calculated from 00:00 UTC, March 31, 2022.

NUMERICAL SIMULATIONS

Numerical simulations were carried out with Comsol Multiphysics software using the deviatoric model of linear viscoelastic material with Maxwell rheology. We assumed linear change of the elastic modulus from 1 GPa at the ice bottom ($z = 0$) to 4 GPa at the ice surface ($z = 80$ cm) (Marchenko, 2024). The Poisson's ratio was set to 0.3. The relaxation time changed linearly from 100 s at the ice bottom to 1000 s at the ice surface (Marchenko et al, 2021). The computational domain was a disk with a radius of 100 m and a height of 0.8 m (Fig. 8). Elastic foundation below the disk with the coefficient $\rho_w g$ imitated the hydrostatic force. Here $\rho_w = 1030$ kg/m^3 is sea water density, and $g = 9.81$ m/s^2 is the gravity acceleration. The radial and vertical displacements were taken equal to zero at $r = 100$ m. The vertical downward force of 4.5 t was applied in the centre of the computational domain over the circle with a

diameter of 4 m. The force was smoothed over 1 m distance around $r = 2$ m. The force increased from 0 to 4.5 t over 10 s. The initial conditions specify zero deformations and zero stresses. We used mapped mesh with 20 elements in the vertical direction and 200 elements in the horizontal directions by $r < 2$ m, and 200 elements with linear growth in the horizontal directions by $2 < r < 100$ m. The simulations of the axially symmetric problem were run for 10 h of physical time.

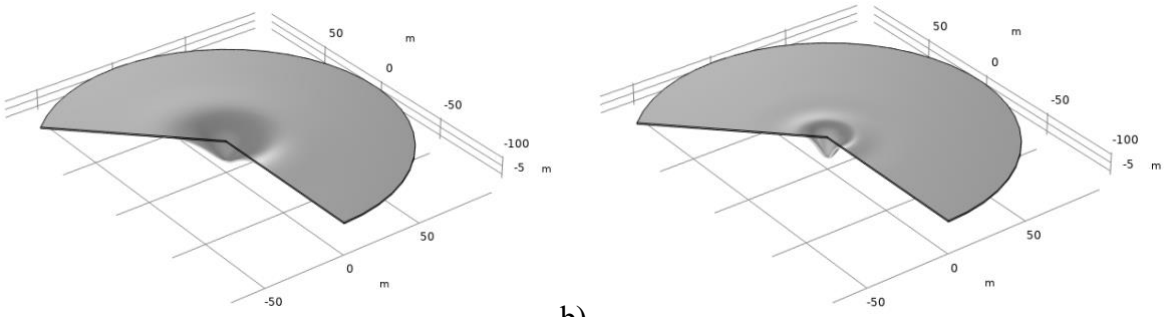

a) b)

Figure 8. Shape of ice surface calculated at $t = 10$ min (a) and $t = 10$ h (b).

Figure 8 show the shape of ice surface calculated at $t = 10$ min (a) and $t = 10$ h (b). The amplitude of the ice surface displacement increases with time in the centre of the computational domain, and the radius of the area with significant bending deformations decreases with time. Figure 9a shows the shape of ice surface in more details. The maximal amplitude of vertical displacement reached 11 cm at $r = 0$ and $t = 10$ h. The black lines in Figure 3b, showing the differences in displacements at $r = 0$ and $r = 5$ m (h_{12}) and at $r = 0$ and $r = 10$ m (h_{13}), were reconstructed using the data of numerical simulations.

Figures 9b and 9c show that significant radial stresses σ_{rr} were distributed over a circle with radius of 40 m with local extremums at $r = 20$ m by $t = 10$ min. After 10 hours, significant radial stresses were distributed over a circle with a radius of 20 m with local extremums at $r = 10$ m. Figure 9d shows the vertical profile of radial stresses at $r = 0$ in different times. Zero radial stresses were calculated at $z = 0.55$ m. The maximum compressive stresses on the ice surface decreased from 50 kPa to 35 kPa when the time changed from $t = 10$ min to $t = 10$ h. Maximal tensile stresses are calculated at $z = 0.3$ m. They decreased from 14 kPa to 8 kPa with a change in time from $t = 10$ min to $t = 10$ h. The nonlinear vertical profile of radial stresses is caused by the influence of vertical profiles of the elastic modulus and relaxation time (Kerr and Palmer, 1972). Figure 10a shows vertical profiles of radial stresses at $r = 4$ m in different times. Their absolute values are smaller than in Fig. 9d. Figure 10b shows the radial stresses versus time calculated at $r = 4$ m with the values of z pointed out in the figure. Radial stresses were about 2-3 kPa at $r = 4$ m and $z = 0.6$ m at time $t < 0.5$ h. This corresponds to an increase in ice pressure of 2 kPa measured by IP1 upon the arrival of BV at the experimental site (Fig. 5c).

Figure 11 shows that the shear stresses σ_{rz} are significantly less than the radial stresses. Shear stresses reach local maxima at $r = 2$ m and $z = 0.55$ m. The maximum shear stress is very stable during the simulation period compared to the local maxima of the radial compressive and

tensile stresses. The viscous dissipation rates shown in Fig. 12 are mainly related to the dissipation of radial deformation energy. The viscous dissipation rates have two local maxima near the ice surface and at $z = 0.3$ m.

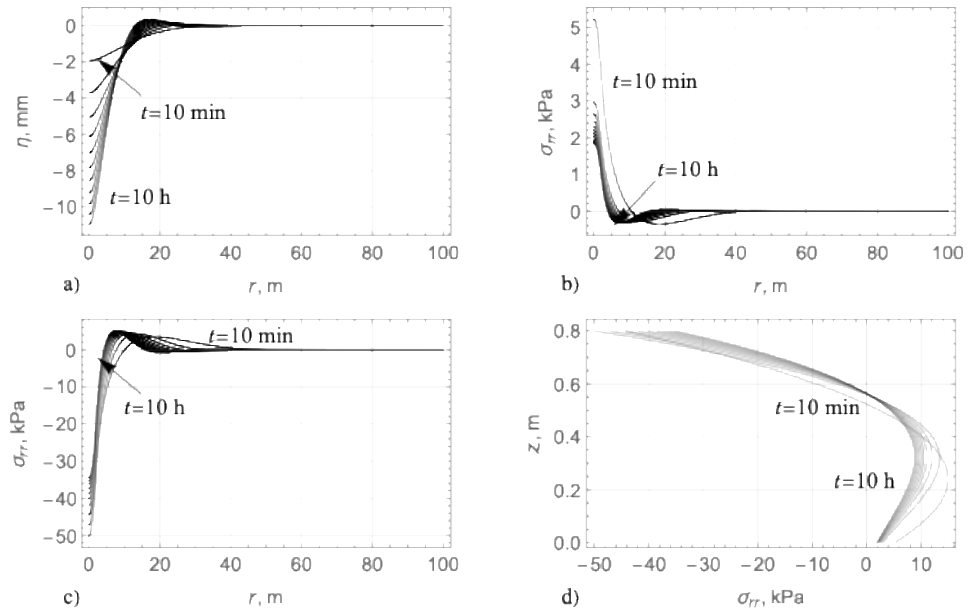

Figure 9. Ice surface shape $z = \eta(r,t)$ over each hour from $t = 10$ min to $t = 10$ h (a). Radial stress $\sigma_{rr}(r,z,t)$ at the ice bottom at $z = \eta(r,t)$ (b) and the ice surface at $z = \eta(r,t) + 0.8$ m (c) at the same times. Vertical profiles of $\sigma_{rr}(r,z,t)$ at $r = 0$ at the same times (d). Positive and negative stresses correspond to extension and compression.

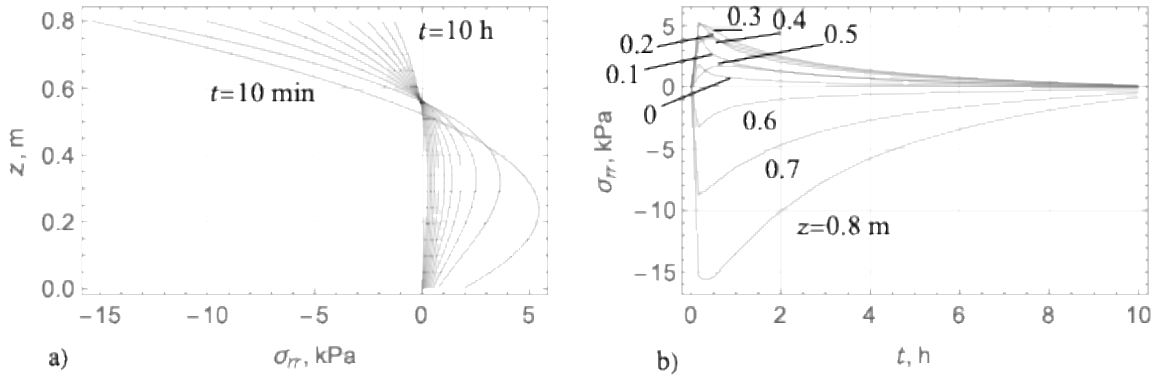

Figure 10. Vertical profiles of $\sigma_{rr}(r,z,t)$ at $r = 4$ m over each hour from $t = 10$ min to $t = 10$ h (a). Radial stresses $\sigma_{rr}(r,z,t)$ at $r = 4$ m versus time, values of z are pointed out (b).

Numerical simulations were also performed for a purely elastic sea ice model with the same thickness and elastic properties. A stationary problem of ice deflection under a load 4.5 t distributed over a circle with a radius of 2 m was considered. The computational domain, boundary conditions and mesh were the same for the elastic and viscoelastic ice models. The simulation was performed in Comsol Multiphysics.

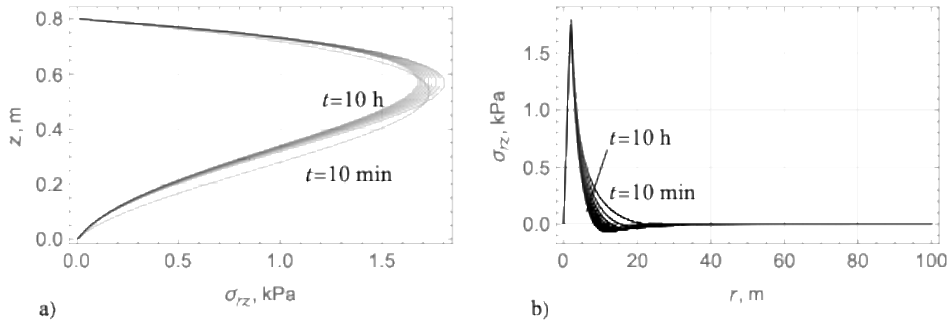

Figure 11. Vertical profiles of $\sigma_{rz}(r,z,t)$ at $r = 2$ m over each hour from $t = 10$ min to $t = 10$ h (a). Shear stress $\sigma_{rz}(r,z,t)$ versus r by $z = 0.55$ m at the same times (b).

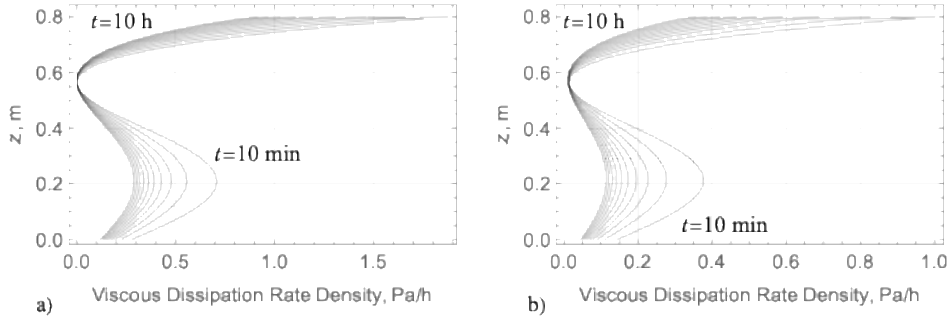

Figure 12. Vertical profiles of the viscous dissipation rate densities calculated over each hour at $r = 0$ (a) and $r = 2$ m (b) from $t = 10$ min to $t = 10$ h.

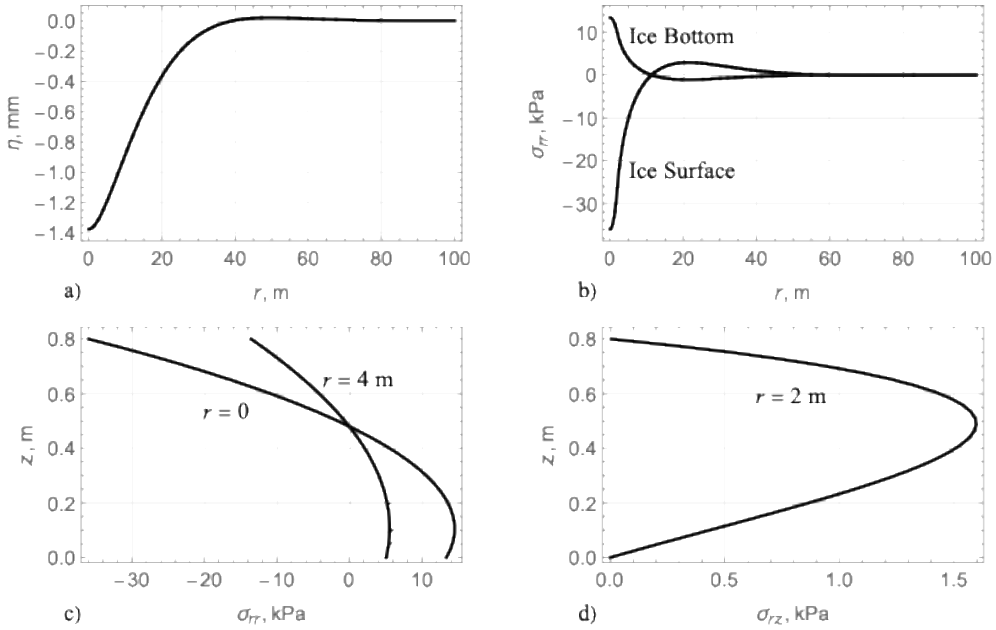

Figure 13. Steady elastic problem. The elevation of ice surface (a) and radial stresses at the ice surface and its base (b). The vertical profiles of radial stresses at $r = 0$ and $r = 4$ m (c) and shear stresses at $r = 2$ m (d).

Figure 13 shows the elevation of the ice surface (a), radial stresses on the ice surface and at its base (b), the vertical profiles of radial stresses at $r = 0$ and $r = 4$ m (c), and the vertical profile

of shear stresses at $r = 2$ m (d). The amplitude of the ice surface elevation of 1.4 mm is significantly less than that shown in Fig. 9a for the viscoelastic ice model. The maximum tensile radial stress at the base of the ice 14 kPa is greater than the radial stresses shown in Fig. 9b for the viscoelastic ice model. The maximum pressure at the ice surface of 36 kPa is less than the ice pressure of 50 kPa calculated at $t = 10$ min for the viscoelastic ice model (Fig. 9d). Figures 11a and 13d show that the maximum shear stresses are the same for the viscoelastic and elastic models of ice.

4. CONCLUSIONS

A full-scale experiment showed the development of ice deflection over ~35 h under the action of a constant load of 4.5 t on the ice surface. We measured the increase in ice deflection below BV on 8 mm and the reduction in the area of deformed ice towards BV during the first 9 hours of the experiment. During the next 20 h the deflection below BV varied in the range from 5 mm to 8 mm. During this time, the area of deformed ice increased and acquired to conical shape. These changes in ice shape can be explained by the influence of thermal deformations of ice due to weather changes. The maximum ice deflection decreased to 3 mm after BV left the experimental site. The ice shape became flatter 5 hour after BV left the experimental site. We measured the increase in ice pressure of 2-3 kPa at a depth of 20 cm below the ice surface near BV upon the BV's arrival at the test site. During the next 9 hours of the experiment, changes in ice pressures correlated well with the ice temperature. The maximum ice pressure 10 kPa over that time exceeded the pressure increase upon the BV's arrival at the test site. This confirms the significant influence of thermal stresses on the bearing capacity of sea ice.

Acoustic activity was registered for 1 h after BV arrived at the test at 9:40 UTC, and also after 13:00 UTC on March 31, 2022. Right at the moment of arrival, we recorded two powerful acoustic pulses, the energy of which was significantly higher than in other events. Acoustic activity after 13:00 UTC correlate well with decreasing air and ice temperatures and is associated with thermal cracking. The two strong acoustic pulses shown in Fig. 7c and 7d could be related to the formation of cracks in the ice bottom, as we didn't observe any cracks on the ice surface. The cracks in the ice bottom were probably refrozen due to the low ice temperature and had no effect on ice deformations in the experiment.

Numerical simulations were performed in Comsol Multiphysics software using Maxwell rheology defined by the elastic modulus, Poisson's ratio and stress relaxation time. In the simulations the elastic modulus changed linearly from 1 GPa at the ice-water interface to 4 GPa on the ice surface, and the stress relaxation time changed linearly from 100 s at the ice-water interface to 1000 s on the ice surface. These values were measured in field tests and in laboratory conditions using ice samples collected from the experimental site (Marchenko et al, 2021; Marchenko, 2024).

The ice shape and ice pressure measurements were consistent with the results of numerical simulations conducted over 10 h of physical time. The simulations showed a decrease in the area of deformed ice and localization of the viscous dissipation rate near the loading region with time. The strain energy criterion of ice failure proposed by Betlaos (1978) is related to the development of creep deformations in ice in the loading area. Over time, this may affect local

ice failure. The most significant contribution of radial stresses is into viscous energy dissipation. The shear stresses along the perimeter of the loading area are quite stable, but they are significantly less than the radial stresses in the centre of the loading area. The mechanism of shear ice failure requires further analysis.

REFERENCES

Betlaos, S., 1978. A strain energy criterion for failure of floating ice sheets. *Canadian Journal of Civil Engineering*, 5(3), 352-361.

Betlaos, S., 2002. Collapse of floating ice covers under vertical loads: test data vs. theory. *Cold Reg. Sci. Techn.*, 34, 191-207.

Cole, D.M., 2020. On the [physical basis for the creep of ice: the high temperature regime. J. Glaciol., 1-14.

Kerr, A.D., Palmer, W.T., 1972. Deformation and stresses in floating ice plates. *Acta Mech*., 15.

Kerr, A.D., 1996. Bearing capacity of floating ice covers subjected to static, moving, and oscillatory loads. *Appl. Mech. Rev*., 49(11), 463-476.

Marchenko, A., Karulin, E., Chistyakov, P., 2021. Experimental investigation of viscous elastic properties of columnar sea ice. *POAC21-043*.

Marchenko, A., 2024. Elastic moduli of first-year sea ice calculated from tests with vibrating beams. *Ocean Modelling*. https://doi.org/10.1016/j.ocemod.2024.102365

Nevel, D.E., 1966. Time dependent deflection of a floating ice sheet. CRREL, *Research Report 136.*

Schulson, E.M., Duval, P., 2009. Creep and Fracture of Ice. University Press, Cambridge.

Sinha, N.K., 1978. Rheology of columnar grained ice, Exper. Mech., 18, 464-470.

Vaudrey, K.D., 1977. Ice engineering: study of related properties of floating sea-ice ice sheets and summary of elastic and viscoelastic analyses. *Technical Report 860*. Civil Eng. Lab., Naval Constr, Bat. Center, Port Hueneme, California 9304.